Journal of Nuclear Materials 406 (2010) 152–165

Contents lists available at ScienceDirect

Journal of Nuclear Materials

journal homepage: www.elsevier.com/locate/jnucmat

# TEM observations and finite element modelling of channel deformation in pre-irradiated austenitic stainless steels – Interactions with free surfaces and grain boundaries

Maxime Sauzay [a,*], Karine Bavard [a], Wade Karlsen [b]

[a] DEN-DMN-SRMA, CEA, bât. 455, 91191 Gif-sur-Yvette cedex, France
[b] VTT Technical Research Centre of Finland, Kemistintie 3, 02044 VTT, Finland

A B S T R A C T

Transmission electron microscopy (TEM) observations show that dislocation channel deformation occurs in pre-irradiated austenitic stainless steels, even at low stress levels (~175 MPa, 290 °C) in low neutron dose (~0.16 dpa, 185 °C) material. The TEM observations are utilized to design finite element (FE) meshes that include one or two "soft" channels (i.e. low critical resolved shear stress (CRSS)) of particular aspect ratio (length divided by thickness) embedded at the free surface of a "hard" matrix (i.e. high CRSS). The CRSS are adjusted using experimental data and physically based models from the literature. For doses leading to hardening saturation, the computed surface slips are as high as 100% for an applied stress close to the yield stress, when the observed channel aspect ratio is used. Surface slips are much higher than the grain boundary slips because of matrix constraint effect. The matrix CRSS and the channel aspect ratio are the most influential model parameters. Predictions based on an analytical formula are compared with surface slips computed by the FE method. Predicted slips, either in surface or bulk channels, agree reasonably well with either atomic force microscopy measures reported in the literature or measures based on our TEM observations. Finally, it is shown that the induced surface slip and grain boundary stress concentrations strongly enhance the kinetics of the damage mechanisms possibly involved in IASCC.



## 1. Introduction

Strain localization occurring at the grain scale has been extensively observed in a variety of metals and alloys subjected to post-irradiation tensile tests. Proton or neutron irradiation with dose higher than a few tenths of dpa was applied [1–7]. In this dislocation channel deformation (DCD), plastic slip is localized in channels having a thickness smaller than a few hundred nm and a length equal to the grain size, i.e. generally a few tens of microns. The onset of DCD is thought to be responsible for the localized necking and sharp reduction in uniform elongation observed in higher dose materials. The degree of localization can be quite high, and can be evaluated using the ratio between the channel and macroscopic axial plastic strains. Following the atomic force microscopy (AFM) measurements of Jiao et al. [5], this ratio is higher than 10 for austenitic steels subjected to post-irradiation tensile loading (macroscopic axial strain of 0.03). The transmission electronic microscopy (TEM) observations of Sharp [1] and Edwards et al. [4] concerning either single crystals or polycrystals of copper subjected to post-irradiation tensile loading allowed these authors to evaluate the extent of plastic strain in the channel. The degrees of localization they obtained were also about 10.

Interactions between mobile dislocations and irradiation-induced defects (proton or neutron irradiation) have been studied in austenitic stainless steels [7]. Irradiation induces displacement damage and interstitial Frank-loop formation. Post-irradiation deformation produces glide dislocations, generally pairs of Shockley partial dislocations. Complex reactions occur between the gliding dislocations, leading to unfaulting and removing of the irradiation defects. This mechanism results in thin defect-reduced channels which are sometimes called "clear bands" [7]. When viewed edge-on in a thin foil such a region appears as a narrow clear channel on the order of 50–200 nm in thickness [7], but in the bulk material it is in fact a thin slab of softer material, constrained on its edges by the grain boundaries, and above and below it by the still-hardened matrix. Further dislocation glide is then focused at those channels, accommodating significant amounts of deformation in a few, very localized bands. That results in intense shear bands that emerge at the specimen surface.

The mechanisms of interaction of mobile dislocations with irradiation-induced defects in copper (stacking fault tetrahedra) have recently been modelled by molecular dynamics [8]. Shearing of Frank loops by edge mobile dislocations and unfaulting by mobile

* Corresponding author.
E-mail address: maxime.sauzay@cea.fr (M. Sauzay).

0022-3115/$ - see front matter © 2010 Elsevier B.V. All rights reserved.
doi:10.1016/j.jnucmat.2010.01.027

screw dislocations were studied by Nogaret et al. using molecular dynamics applied to a material with a stacking fault energy close to that of 316L at 300 °C [9]. Their aim was to evaluate the resolved shear stress required for channel formation. Because of the abrupt strain softening and subsequent minimal additional strain hardening associated with DCD, the origin and operation of the dislocation channels is of great importance to better understanding (and predicting) the deformation behaviour of irradiated materials. Edwards and Singh have recently carried out a study specifically examining the evolution of cleared channels in neutron irradiated pure copper as a function of tensile strain, via interrupted tensile tests [10]. They found that channels were present in a low number even *before* the macroscopic yield point. New primary channels and secondary channels then continued to form with increasing strain. The slight strain hardening observed was related directly to the initiation of new channels as earlier sources were exhausted. Some of the channels were observed to penetrate through both the twin boundaries and grain boundaries, but others were stopped at such obstacles. However, the exact mechanism of channel initiation and their subsequent evolution as a function of strain still remains poorly understood [4].

Despite a lack of consensus on the exact mechanism underlying channel behaviour, it seems very likely that the interaction of channels with grain boundaries causes local damage by shear displacements and/or stress/strain concentrations. This would be as a result of the dislocations generated at one source boundary being deposited at the site where the channel ends, at the other boundary. Such locations could then become potential crack nucleation sites, promoting fracture along grain boundaries. Indeed, Toivonen et al. observed thin, regularly-spaced slip lines emerging at the grain-boundary surface of the intergranular fractures of a highly-irradiated 304 stainless steel following room temperature tensile testing [12]. Clear bands impinge on grain boundaries. This induces stress or plastic strain concentrations, as shown by TEM observations on copper polycrystal deformed after neutron irradiation [4]. Edwards et al. observed either local lattice rotations corresponding to high elastic strain concentrations or considerable amount of (plastic) shearing at the grain boundary if another channel formed on the opposite side of the grain boundary [4]. Such propagation of a channel in the neighbouring grain was often observed [5]. The higher the remote strain, the more clear bands propagated across the grain boundaries.

Because of these interactions with grain boundaries, clear bands are often considered to promote grain boundary crack initiation and propagation, and therefore be of importance to irradiation assisted stress corrosion cracking (IASCC) [10,4]. Many factors are thought to be involved in IASCC too though, including corrosion and irradiation induced segregation at grain boundaries [11,13]. Nonetheless, the observation of intergranular cracking in high-dose materials tested even in an argon environment, demonstrates the relative importance of mechanical aspects such as DCD.

Several computational studies have tried to evaluate the plastic slip inside thin slip bands. Authors first modelled bulk slip bands as elongated inclusions embedded in a matrix which mimics the whole polycrystal [14]. This allowed them to use the analytical solution given by Eshelby for bulk inclusion [15]. Then, Finite Element computations using crystalline plasticity allowed the introduction of surface effects [16–18]. In the case of type B slip bands, both slip magnitude and heterogeneity are considerably enhanced by surface effects [17,18]. The corresponding slip system is well-oriented and shearing occurs through the free surface.

But there has been little work published that is dedicated to the evaluation of strain concentrations at the free surface or in the vicinity of grain boundaries induced by channel deformation. TEM observations allow us to evaluate channel characteristics and local slip in an austenitic stainless steel pre-irradiated at a low dose. Channels are then modelled by thin slip bands having a CRSS that is much smaller than that of the surrounding matrix or grains. Finite Element (FE) computations are carried out for remote strains as high as 0.01. A parametric numerical study of the influence of the microstructure or constitutive law parameters permits us to evaluate which parameters are the most influential. A general analytical formula, validated by a large number of FE computations is then given together with its validity domain. The computed surface slips are compared with AFM measures in austenitic polycrystals subjected to post-irradiation tensile deformation [5], while the computed local slips at an interior grain boundary are compared to measures obtained using the TEM pictures presented below. Finally, the potential consequences for crack initiation are discussed.

## 2. TEM observations and corresponding modelling hypothesis

### 2.1. TEM observations

Appropriate model development must rely on experimental observations in order to parameterize and verify the model. However, while channel deformation is most prevalent in high-dose materials, such materials exhibit chaotic image contrasts in transmission electron microscope (TEM) images, reducing the visibility of other features in the microstructure that may otherwise be exploitable in characterizing the deformation bands. Examinations carried out on less-extensively irradiated austenitic stainless steel have found that, even at only 0.11 dpa of irradiation, the general microstructural features like pre-existing linear dislocations, new dislocations, precipitates, and twin and grain boundaries can still be readily imaged, yet the radiation-induced defect population is still adequate to promote channel deformation [21]. Thus, in order to guide the modelling hypotheses, consideration here is given of the deformation microstructure of a 304L stainless steel material irradiated to 0.16 dpa ($1.1 \times 10^{20}$ n/cm$^2$, $E > 1$ MeV) and then mildly strained to initiate channels. Neutron irradiation took place at 185 °C and tensile loading at 290 °C. The maximum principal applied stress experienced by the examined volume was evaluated by FE computations to be about 150–200 MPa [21]. The bulk tensile yield stress of the material was about 300 MPa.

The dislocation channel deformation in the 0.16 dpa material is shown in Fig. 1. While channels are not typically reported for such

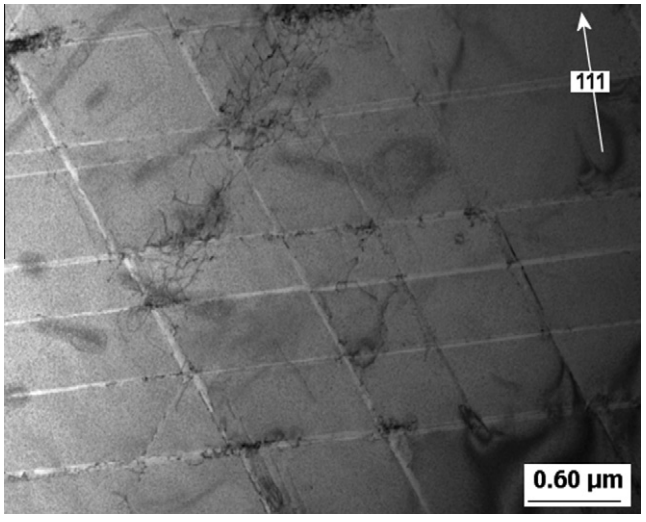


**Fig. 1.** The dislocation channel structure of a 0.16 dpa 304L stainless steel following mild deformation. The incident beam direction is [1 1 0] and the diffraction vector is plotted.

low-dose materials, their defect-cleared nature is evident, especially when viewed closer to an edge-on orientation and at higher magnification, as illustrated in Fig. 2. Since the reduced population of fine irradiation defects in the band reduces the extent of scattering of the electron beam, the band stands out brighter against the surroundings. Also illustrated in Fig. 2 is the fact that the selected area diffraction (SAD) pattern of the band has no other reflection than that of the surrounding matrix, demonstrating that it has the same lattice structure. The cleared channels span the entire grain, so their length is equivalent to the material grain size, about 100 μm in this case. The spacing of the channels in Fig. 1 varies between 0.2 and 1.2 μm, but on average is about 0.6 μm. However, the number of channels typically increases with increasing strain, thereby reducing the average spacing. The most significant parameter is generally deemed to be the thickness of the channel, $h$. In this case the thickness varies between 20 and 60 nm. The channel length, $L$, is usually close to the grain size, as experienced by our TEM observations. That would produce an $h/L$ ratio of approximately 2400. In comparison to more highly irradiated materials, the channels observed in this material are thinner and more closely spaced, while the large grain size of the material results in an exceptionally high aspect ratio for the channels. As will be shown in the modelling part, this would be expected to strongly affect the extent of slip localized to the channel.

The extent of strain localization due to channel deformation is evident at features such as pre-existing dislocations in the matrix, where their intersection by a band results in a step being formed. The intersection of one band by another also shows evidence of such local straining in the band. Examples of those features are shown in Fig. 3. Calculation of the transposition of the feature in the direction parallel to the channel on each side of the channel gives an estimate of relative displacement along the channel due to shearing. Such calculations yield step sizes of 40–80 nm, so of a similar magnitude as the thickness of the channels. Similar steps could be observed in Fig. 4, in the shearing of straight dislocation lines. The measured channel thicknesses and relative displacements will allow us to evaluate the experimental local slip (displacement divided by thickness), considering FCC easy slip systems $\{1\,1\,1\}\langle -1\,1\,0\rangle$. Together with the grain size, they will be used in Section 4.2 for computing theoretically the corresponding plastic slips, for comparison with the observations.

As shown in Fig. 5, tilting the specimen slightly brings into contrast the dislocations present in some of the bands. These are predominantly in the form of pile-ups where bands intersect one another. The dislocation pile-ups contained extended stacking faults as well. The formation of extended stacking faults on every other close-packed plane can in fact produce hexagonally-close packed (hcp) epsilon martensite [22]. Additionally, deformation twinning is a mechanism produced by the glide of Shockley partial dislocations of the same sign on *successive* $\{1\,1\,1\}$ planes [7]. Thus, bands not yet containing a significant population of dislocations may not show any other reflections in SAD than the matrix ones, but upon accumulation of stacking faults they may show hcp or even twin reflections. Nonetheless, it has been shown [21] that those features are all related to dislocation glide on the primary slip planes, and could be expected to harden the material in the bands accordingly.

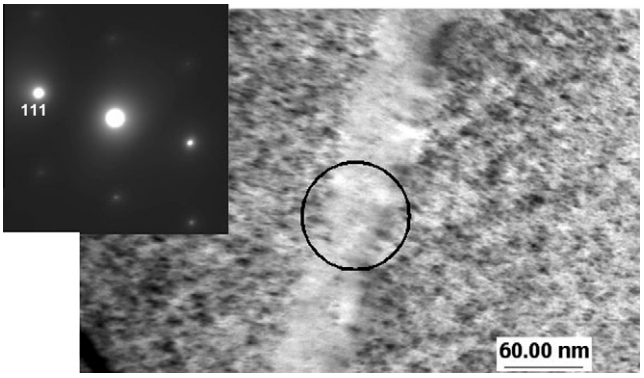


**Fig. 2.** The cleared nature of the band is evident in the distinct lack of irradiation defects. The fact that the selected area diffraction (SAD) pattern of the band has no other diffraction than the 1 1 1-type of the surrounding matrix, demonstrates that it has the same lattice structure as the matrix does. The incident beam direction is [1 1 0]. 304L stainless steel, 0.16 dpa.

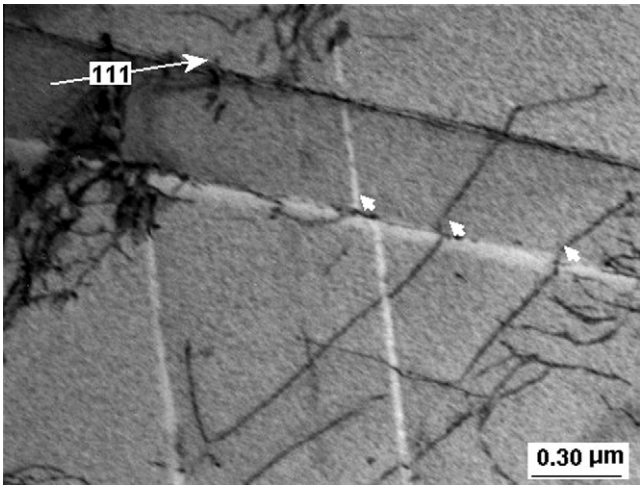


**Fig. 3.** Pre-existing dislocations and other channels that were intersected by a channel typically experienced a step, which demonstrates the local nature of strain occurring within the bands. The thickness of the horizontal channel is 52 ± 8 nm. The displacements along the channel carried out by one of the vertical channel and by two dislocations are respectively: 70 ± 8 nm, 70 ± 8 nm, 65 ± 8 nm (white arrows). The incident beam direction is [1 1 0] and the diffraction vector is plotted. 304L stainless steel, 0.16 dpa.

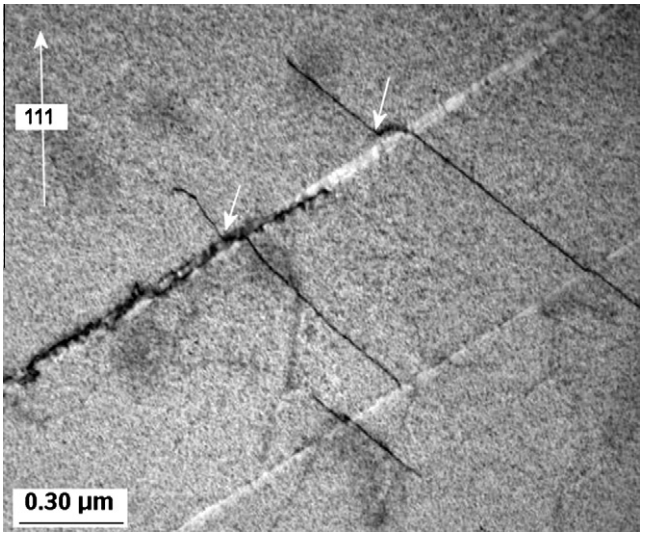


**Fig. 4.** Assuming that the dislocations were initially straight before being intersected by the channel, the size of the jog introduced by the strain in the channel can be compared to the size of the steps produced at the surface in the case of the channel emerging there. The thickness of the upper channel is equal to 40 ± 5 nm. The displacement imposed to the crossed dislocations (white arrows) are equal to 70 ± 5 nm (dislocation) and 55 ± 5 nm. The incident beam direction is [1 1 0] and the diffraction direction is plotted. 304L stainless steel, 0.16 dpa.

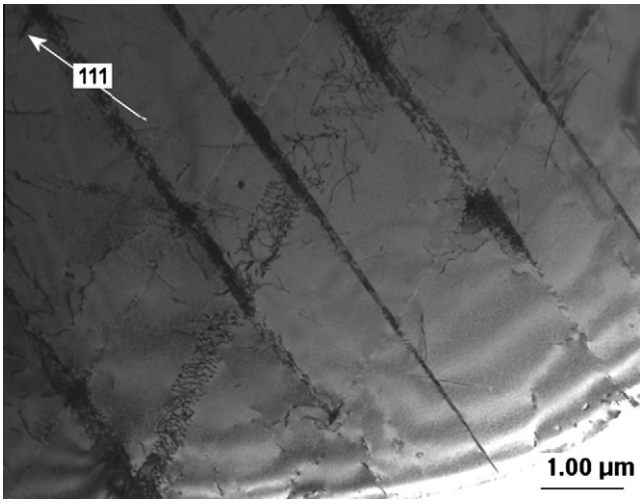


**Fig. 5.** Tilting the specimen foil slightly brings into contrast dislocations present in many of the bands. They are predominantly in the form of pile-ups where bands intersect one another. The incident beam direction is [1 1 2] and the diffraction vector is plotted. 304L stainless steel, 0.16 dpa.

Fig. 6 shows the interaction of a channel with a grain boundary which is deformed due to the channel glide. FE computations will allow us to compare channel slip at the free surface where no constraint effect occurs and at the grain boundaries.

### 2.2. Modeled microstructures

Following the TEM observations, two simple microstructural configurations are considered for computing the channel plastic slips.

#### 2.2.1. Configuration 1 (the simplest one)

One channel is embedded at the free surface of a matrix which mimics the whole polycrystal or single crystal (Fig. 7a and b). This simple configuration allows us to evaluate the stress/strain distribution taking into account crystalline elasticity and (visco)plasticity. The length and thickness of the channel are denoted as $L$ and $h$ (Fig. 7b). The thickness is measured along the $\langle 1\,1\,1\rangle$ axis perpendicular to the channel (see below). For polycrystals, the length $L$ is close to the grain size, as experienced by the TEM observations. The ratio between $L$ and $h$ is generally high (about hundred or even more for large grain sizes). Both plane stress and plane strain conditions are used, using a mesh width which is either very small or very large. The width is defined along the transverse direction i.e. perpendicularly to Fig. 7a. Following several observations in the small strain regime [15,26], the grains containing channels are generally well-oriented, which means that the Schmid factor values are high. As observed for example by Byun et al. [6], the channel is parallel to the easy slip plane. For a face-centred cubic (FCC) metal or alloy, 12 easy slip systems, $(n_i, m_i)$ $i = 1, \ldots, 12$, are defined in each grain. The unit normal vector of the $i$th slip system is denoted as $n_i$ whereas the unit slip vector is denoted as $m_i$. For FCC metals, the slip systems are defined by normal directions $\{1\,1\,1\}$ and slip directions $\langle 1\,1\,0\rangle$. The well-oriented grains present one slip system $(n, m)$ with a Schmid factor equal to its maximal value, 0.5. The resolved shear stress is defined as the maximum shear stress magnitude among those computed on each easy slip system of the considered grain, $|\tau_i| = |m_i^T \sum n_i|$ $(i = 1, \ldots, 12)$. The local and macroscopic stress tensors are denoted as $\sigma$ and $\sum$. The Schmid factor is the ratio between the local resolved shear stress and the remote axial stress, $\sum_{xx}$ (tensile axis, $x$).

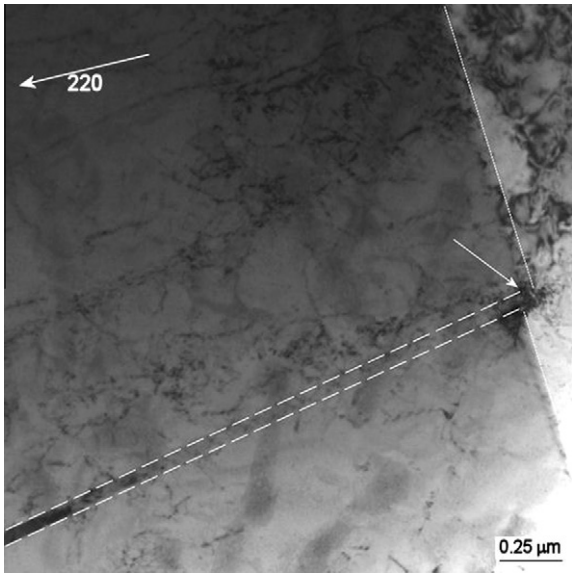


**Fig. 6.** Interaction of a channel with a grain boundary (see the white arrow). The GB is sheared because of the channel glide. The incident beam direction is [1 2 2] and the diffraction vector is plotted. 304L stainless steel, 0.16 dpa.

For the well-oriented grains, both the n and m vectors are inclined at 45° with respect to the tensile direction. In this study, the following directions of the well-oriented slip system have been chosen: $n = 1/3(1, 1, 1)$ and $m = 1/2\,(1, 0, -1)$. Among well-oriented slip planes, type A and type B facets can be distinguished. For type B facets, both vectors are inclined at 45° with respect to the free surface. But, for type A facets, both vectors are located in the free surface. Both facets correspond to well-oriented slip systems. But type B facets induce relief formation whereas type A facets induce only shearing inside the free surface without relief formation. In addition, recent computations showed that type B facets induce higher plastic slip inside well-oriented grains [23] or inside slip bands [19] than type A because of the efficiency of surface effect with respect to the slip direction, m. The microstructure data are given in Table 1.

#### 2.2.2. Configuration 2 (parallel channels)

This configuration takes into account two parallel channels instead of only one (Fig. 8a and b). TEM observations show that several parallel channels are usually observed in the same grain, even in the small strain regime (Figs. 1 and 3–5) [15]. The distance between the channels is denoted as $d$ (Fig. 8b). In our study, the inter-bands spacing, $d$, varies between 0.7 and 3 μm, which corresponds to the distances usually observed (Figs. 1 and 3–5) [5,15,21]. The influence of parallel channels could be investigated (screening effects for example).

For studying the influence of the channel aspect ratio, $L/h$, two different values are used for comparison: either $L/h = 200$ (for example: $L = 10$ μm and $h = 50$ nm, which are suitable values for austenitic stainless steels pre-irradiated at doses higher than a few dpa) and $L/h = 15$ which is more than one order of magnitude smaller. The microstructure data are given in Table 1.

### 2.3. Crystalline constitutive laws

#### 2.3.1. Cubic elasticity

The austenitic stainless steels present a FCC structure. Therefore, cubic elasticity is used at the grain scale for the considered metals. Three elasticity parameters are involved: $C_{11}$, $C_{12}$ and $C_{44}$ [27,28]. The elasticity anisotropy degree of each metal can be estimated by the calculation of a dimensionless coefficient: $a = 2C_{44}/$

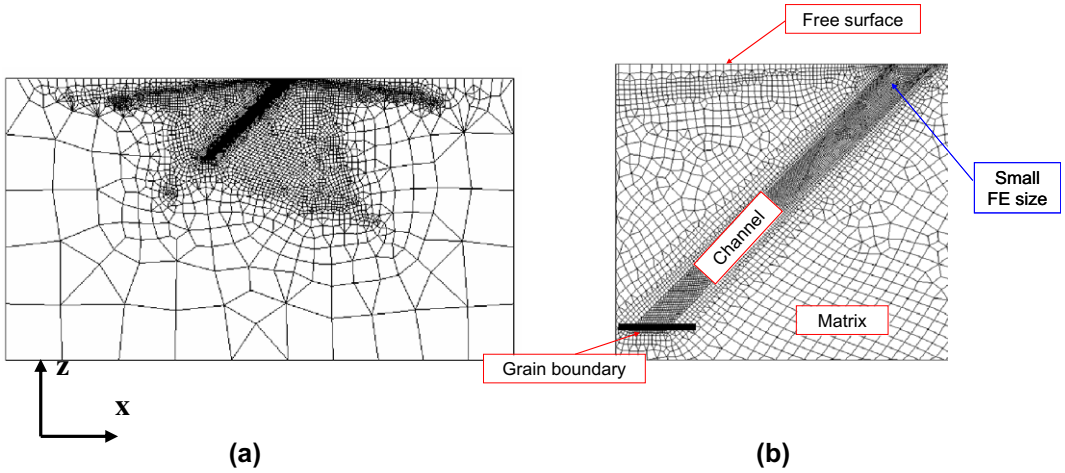


**Fig. 7.** (a) Zoom on the mesh of the matrix containing the surface channel (tensile axis, $x$) and (b) zoom of the surface channel.

**Table 1**
Microstructure lengths used for building the meshes of microstructures 1 (one channel, Fig. 7) and 2 (two parallel channels, Fig. 8) (see Section 2.2).

| Configuration | Grain size, $L$ (μm) | Channel thickness, $h$ (nm) | Inter-channel spacing, $d$ (μm) |
|---|---|---|---|
| Microstructure 1 | 10 | 50–650 | No object |
| Microstructure 2 | 10 | 50–650 | 0.7–3 |

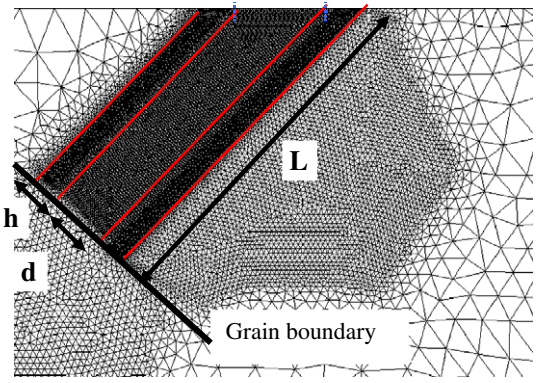


**Fig. 8.** Enhanced mesh for evaluating the effect of another parallel channel.

($C_{11}$–$C_{12}$) [27,28]. With respect to isotropy, austenite is strongly anisotropic ($a = 3.3$ at room temperature). For comparison with experimental measures obtained after deformation at 290 °C, values of the Young's modulus and Poisson ratio of 173 GPa and 0.3, respectively, are used (instead of 200 GPa and 0.3 at room temperature). The temperature dependence of the three elastic constants, $C_{11}$, $C_{12}$ and $C_{44}$, is assumed to be the same as the Young's modulus one. The crystalline elasticity parameters are displayed in Table 2, along with the corresponding anisotropy coefficients and macroscopic isotropic elasticity coefficients, $Y$ and $\nu$. In the following either isotropic elasticity or crystalline elasticity is used for both channel(s) and matrix, in order to evaluate the influence of the anisotropy degree.

**Table 2**
Elastic constants of the studied crystals (GPa) (cubic elasticity), corresponding anisotropy coefficient and macroscopic elasticity coefficients (Young's modulus, $Y$, and Poisson ratio, $\nu$) (isotropic elasticity) [27,28]. Room temperature.

| | $C_{11}$ | $C_{12}$ | $C_{44}$ | $a = \mu_{max}/\mu_{min}$ | $Y_{max}/Y_{min}$ | $Y$ | $\nu$ |
|---|---|---|---|---|---|---|---|
| Fe γ | 197.5 | 125 | 122 | 3.36 | 2.96 | 200 | 0.33 |

*2.3.2. Crystalline viscoplasticity*

As usual, constitutive crystalline viscoplasticity laws are defined by the viscoplastic flow equation and the hardening equation (see for example [29,31]). The viscoplastic flow law gives the dependence of the viscoplastic slip rate ($i$th slip system), $d\gamma_i^{vp}/dt$, with respect to the corresponding shear stress, $\tau_i$. The hardening equation allows the computation of the evolution of the critical shear stress on the $i$th slip system, $\tau_{c,i}$, depending on all the viscoplastic slip rates ($j = 1,12$). Self-hardening ($j = i$) and latent hardening ($j \neq i$) are taken into account through the parameter $q$ ($q > 1$). The equations used in this work are similar to the ones proposed by Anand et al. [29]:

$$\dot{\gamma}_i^{vp} = \dot{\gamma}_0 \left( \frac{|\tau_i|}{\tau_{c,i}} \right)^n sign(\tau_i) \quad \text{whatever the resolved shear stress} \tag{1}$$

$$\dot{\tau}_{c,i} = \sum_{i=1}^{12} h_{ij} |\dot{\gamma}_j^{vp}| \tag{2}$$

$$h_{ij} = H_i \quad \text{if } i = j \quad \text{and} \quad h_{ij} = qH_i \quad \text{elsewhere} \tag{3}$$

$$H_i = H_0 \left( 1 - \frac{\tau_{c,i}}{\tau_{sat}} \right)^a \tag{4}$$

Seven material parameters are used by the viscoplasticity model.

For the sake of simplicity, the effects of viscosity are neglected in the following. The chosen value of the exponent, $n \approx 50$, is so high that the viscosity effect is very weak. For austenitic stainless steels, the influence of viscosity is indeed weak, at least at room temperature ($n = 25$ [29]) and 550 °C ($n = 47.6$ [31]).

The influence of the initial critical shear stress, $\tau_{c0}$, of each considered "phase" will be investigated using physical orders of magnitude given in the literature (see Section 2.3.3). The irradiated matrix is a "hard" phase and the channel is a "soft" phase.

The hardening parameters are similar to the ones given by Anand et al.: $H_0 = 250$ MPa, $a = 2.5$ (or $a = 1$), $\tau_{sat} = 190$ MPa or more, and $q = 1.4$ [29]. This corresponds to weak tensile hardening of copper single crystals. The hardening mechanisms do not seem strong in the channels, as they are not during stage I of tensile deformation of 316L well-oriented single crystals (weak hardening

slope) [32,33]; irradiation defects are quickly removed and are not compensated by dislocation multiplication. It should nevertheless be noticed that this concerns only short-range interactions, because long-range interactions are naturally taken into account in the FE computations. These long-range interactions induce back-stresses due to the surrounding hard grain and matrix. The effect of the pile-ups observed by TEM is neglected in the computations but will be discussed in Section 4 Finally, two extreme cases will be considered for studying the effect of the latent hardening coefficient, $q$. A small value, $q = 1.4$, is used to simulate a situation in which the activation of new slip systems during the tensile loading is possible, so multiple slip is favoured, which is typical of a high stacking fault energy (SFE) material [29]. A very high value, $q = 1400$ is used to simulate a situation in which the activation of a new slip system is impossible, as when planar slip is favoured, which is typical of a low SFE material. This allows the study of the influence of multiple slip versus planar slip.

#### 2.3.3. Evaluation of the initial critical shear stress parameters

As described in the following, the initial critical shear stress values should be ones of the most influential material parameters, because both viscosity effects and hardening are weak.

The soft phase (i.e. channel volume) is considered first. The TEM observations indicated that clear bands are quite free of defects. In addition, the dislocation densities are rather weak. That is why the initial critical shear stresses of single crystals without defects have been used as initial values for the channels. For example, for 316L austenitic stainless steels values of about 33 MPa and 40 MPa have been given by Li and Laird [32] and Gorlier [33], respectively, using mechanical testing of well-oriented, recovered, single crystals at room temperature. A value of 60 MPa was found by Héraud, by adjusting the crystalline parameters for predicting the polycrystalline tensile curve at 550 °C [31].

Secondly, the initial critical shear stress of the hard phase (i.e. irradiation hardened matrix material surrounding the channel and of the neighbouring grains should be chosen as well). In the past, different theoretical approaches have been used for evaluating the required shear stress for allowing a mobile dislocation to overcome the irradiation defects obstructing dislocation glide:

- Bacon and Osetsky used the Orowan formula, which allows the evaluation of the required stress for passing through impenetrable obstacles [34]. Using typical values of high-dose neutron irradiation (40 displacements per atom (dpa)), i.e. Frank loop diameter: 7 nm and density: $6 \times 10^{23}/m^3$ [35], a typical critical shear stress of about 360 MPa is calculated.
- Using the same experimental data, the application of the forest model proposed by Pokor et al. [35] gives a critical shear stress of about 200 MPa.
- Finally, several molecular dynamics (MD) computation results have been recently published. They consider more detailed interactions between one mobile dislocation (faulted or unfaulted) and irradiation-induced defects. For example, Rodney calculated that the required stress for unfaulting Frank loops (diameter 7 nm) by a mobile screw dislocation in nickel at 0 K is about 400 MPa [36]. The temperature dependence has been studied more recently by Ostesky et al. [8]. Concerning interactions with small SFTs (copper, nickel), smaller critical shear stresses were obtained at room temperature. It should finally be noticed that critical shear stresses depend on nature of the defect, orientation, screw/edge mobile dislocation character, distance between the mobile dislocation and the defect... [9,36]. More recently, Nogaret et al. gave a range of 300–600 MPa for the shear stress required for unfaulting of Frank loops in austenitic stainless steels at 300 °C [9].

For being general enough, four different critical shear stresses are used in the hard phase of pre-irradiated austenitic steels: 150, 300, 500 and 1000 MPa. The smallest critical stress, 150 MPa, is equal to one-half of the macroscopic yield stress measured after neutron irradiation with a dose of 0.16dpa and tensile loading of a 304L specimen [37] in the conditions described in [21].

### 2.4. Finite Element computations

The FE code Cast3m [38] is used as well as subroutines developed by Héraud [31,39] for developing crystalline constitutive laws. They have been used recently for studying the influence of crystalline elasticity on the resolved shear stress distribution at the free surface of multicrystals [40,41]. The meshes are 3D ones, made of tetrahedra. The displacements (degrees of freedom) are computed at each of the vertices of the tetrahedra. The stress and strain tensors are computed at each Gauss point of each finite element of the mesh. Whatever the modelled configuration, the matrix is much larger than the channel length (Fig. 7a). For building the 3D meshes, 2D meshes are extruded along the $y$ axis, perpendicularly to the tensile axis, $x$, and the $y$ axis perpendicular to the free surface (Fig. 7a). The extruded 3D meshes are either narrow or deep in order to mimic either plane stress or plane strain hypothesis. The depth along the $y$ axis is equal to either the channel thickness or the grain size. In fact, only the ratios between considered lengths affect the stress values. The mesh is particularly refined in the vicinity of the grain boundary and channel. Its quality was checked carrying out computations with a finer grid. Relative numerical errors on surface and grain boundary slips are smaller than a few percents. The time discretization has been checked to be fine enough as well. Uniform horizontal uniaxial displacements are prescribed along the $x$ axis, at both matrix lateral faces which are perpendicular to the tensile axis, $x$. The displacements along the $x$ axis applied on these left and right lateral faces are equal to respectively zero and the product between the mesh length and remote strain. The maximum total remote strain depends on the material and loading condition, but is smaller than 0.01. This corresponds generally to the elastic regime at the macroscopic scale. The four other faces are traction free. Some other node displacements located in the ($y = 0$) plane are fixed in order to avoid rigid body motion indetermination, the node at the bottom of the left lateral face is fixed in the three directions and the node at the top of the opposite lateral face is fixed in the $y$ direction.

## 3. Results of the finite element analysis

### 3.1. Slip activity

The evolution of primary plastic slip activity with respect to the remote stress, $\sum_{xx}$, is now described for the low aspect ratio value. In the following, the deformation of a pre-irradiated specimen is modelled. High-dose irradiation leads to typical values of $\tau_{c,channel} = 60$ MPa, $\tau_{c,matrix} = 1000$ MPa. The aspect ratio is: $L/h = 15$. The deformation-induced surface step obtained for a high applied stress is shown in Fig. 9a. The distribution of plastic slip is in fact very heterogeneous (Fig. 10a). Whatever the applied load, the primary slip is higher in the vicinity of the free surface than in the bulk of the channel (Fig. 9b). The slip in the vicinity of the grain boundary is much smaller than at the free surface. Fig. 9b and a, plotted using a magnitude applied to the displacement fields of respectively 4 and 1, can be compared. This difference is due to the constraint effect induced by the hard material surrounding the grain boundary. The higher the remote stress, the stronger the slip heterogeneity and the surface slip concentration. As expected, the slip values increase with increasing applied load (Fig. 11a and b).

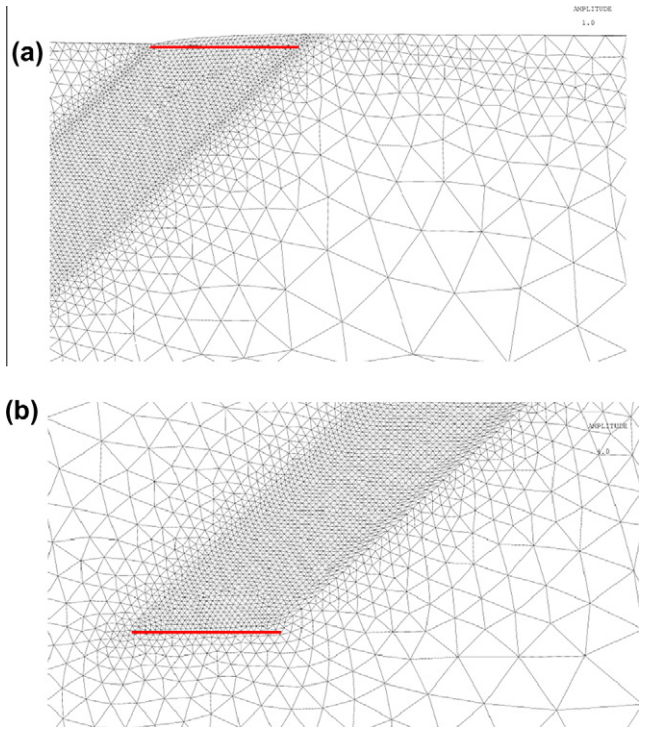


**Fig. 9.** (a) Deformation-induced surface relief of the channel (magnitude $*$ 1); (b) deformed grain boundary (magnitude $*$ 4). Austenitic steel, 300 °C. Critical shear stresses: $\tau_{c,channel}$ = 60 MPa and $\tau_{c,matrix}$ = 1000 MPa. Latent hardening coefficient: $q$ = 1.4. Plane stress. Macroscopic axial stress: $\sum$ = 780 MPa, macroscopic axial strain: E = 0.45%. Channel/matrix mesh, $L/h$ = 15.

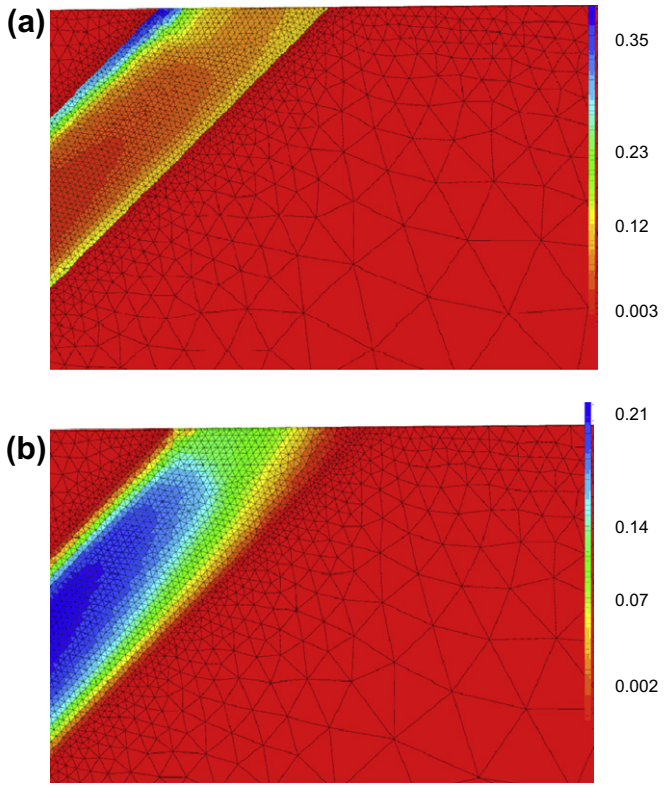


**Fig. 10.** Isovalues of (a) the primary viscoplastic slip; (b) the secondary viscoplastic slip (zoom of the free surface). Austenitic steel, 300 °C. Plane stress. Critical shear stresses: $\tau_{c,channel}$ = 60 MPa and $\tau_{c,matrix}$ = 1000 MPa. Latent hardening coefficient: $q$ = 1.4. Macroscopic axial stress: $\sum$ = 780 MPa, macroscopic axial strain: E = 0.45%. Channel/matrix mesh, $L/h$ = 15.

For the remote stress of $\sum$ = 780 MPa, a maximum primary slip value of 0.35 is reached, which corresponds to a very intense shear in the vicinity of the free surface.

### 3.2. Influence of (visco)plasticity parameters

Even for a very small remote stress, multiple slip is observed if a typical value of the latent hardening ratio is used (for example $q$ = 1.4 [29], see Eq. (3)). Contrary to the case of single crystals (without neighboring grains or surrounding matrix), not only the primary slip system (number 1) but also the secondary system (number 5) is activated (Fig. 10b). Rotation of the crystallographic axis induced by large slips could enhance activation of the secondary slip systems [29] but the effect of this rotation is negligible for small slip values. Therefore, multiple slip activity is mainly due to residual stresses induced by the strain incompatibilities between the (soft) channel and the (hard) surrounding matrix. Strain incompatibilities are indeed known to increase triaxiality, which favours the activation of secondary slip systems. Nevertheless, the primary viscoplastic slip in the vicinity of the free surface remains higher than the secondary slip regardless of the applied stress (compare Fig. 10a and b). A similar FE computation was carried out, assuming that the latent hardening coefficient is 1000 times higher than the coefficient used previously. Using this high coefficient value, $q$ = 1400, it is noted that only primary slip system is activated, while the slip values computed on all the other slip systems are negligible, i.e. planar slip is favoured. Nevertheless, the computed maximum and mean surface primary slips are very close to the values computed in the case of multiple slip ($q$ = 1.4). Table 3 gives the mean surface and mean grain boundary slip values obtained for particular combinations of material parameters. These mean values are obtained by dividing the relative displacement (between the left and right corners of the channel and computed along the primary slip vector, $m$) by the channel thickness, h (Fig. 7b). The same definition is used by Jiao et al. [5]. These mean surface and grain boundary slips take into account the activities of all slip systems as well as elastic transformation because they are based on the computed values of the displacements of the points located at the corners of the channel, either at the free surface or at the grain boundary. It should be noticed that the usual FE size is small enough to get surface and grain boundary slips which do not depend on the FE size (Fig. 11a and b).

Following Table 3, the effect of latent hardening on the deformation-induced steps is negligible. The effect of crystallographic rotation during loading induces variations of the Schmid factor but this does not affect mean surface and grain boundary slip values (Table 3). As detailed in the discussion, these surface steps can be measured experimentally and compared with computed values. The shapes of the surface steps can be compared as well. Finally, the influence of the matrix critical shear stress of the surface or grain boundary slip can be studied using Table 3 and Figs. 11a and b and 12. The considered critical shear stresses belong to the ranges given by either experimental studies or atomistic computations:

- As the channels contain few defects and dislocations, their critical shear stresses are assumed to have the same orders of magnitude as single crystals in the recovered condition.
- Critical shear stresses in the matrix or in the surrounding grains (material with a large density of irradiation-induced defects) have the same orders of magnitude as the shear stress for the clearing of defects by mobile dislocations [9,34–36].

Whatever the channel aspect ratio, the influence of channel critical shear stress is negligible if the applied tensile stress is much higher than two times the channel critical shear stress, which is

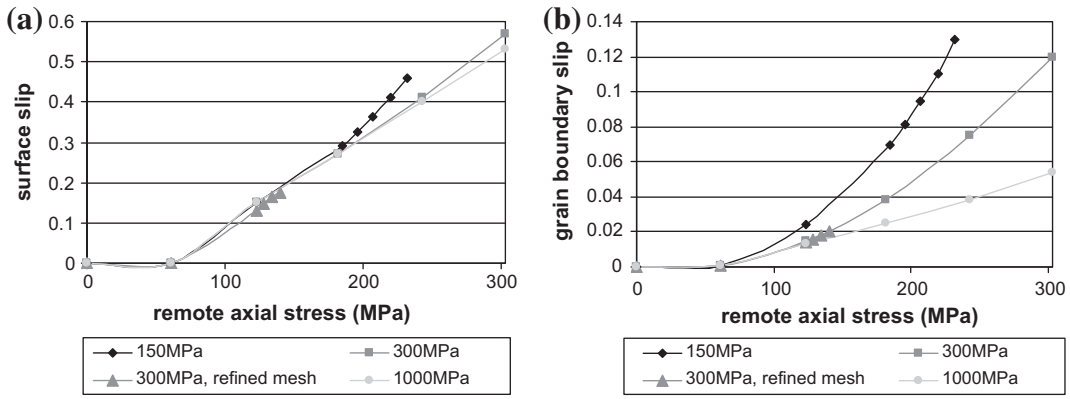


**Fig. 11.** Influence of the matrix critical shear stress on the slip: (a) at the free surface and (b) at the grain boundary. Channel critical shear stress, $\tau_{c,channel}$ = 30 MPa. Austenitic steel, 300 °C. Channel/matrix mesh, $L/h$ = 200.

**Table 3**
Material parameters defining the plastic behaviours of the channel and matrix. Corresponding computed slip values (at the channel free surface or at the grain boundary). Austenitic stainless steel subjected high-dose pre-irradiation leading stabilization of the irradiation hardening with respect to the dose (see Section 2.3.3). Macroscopic axial stress: $\sum$ = 780 MPa; 300 °C. Channel–matrix mesh. Channel aspect ratio: $L/h$ = 15.

| Computation case | $\tau_{c,channel}$ (MPa) | $\tau_{c,matrix}$ (MPa) | Hardening coefficient (MPa) | Latent hardening coefficient, $q$ | Rotation of the crystallographic axis | Mean surface plastic slip | Mean grain boundary plastic slip |
|---|---|---|---|---|---|---|---|
| 1 | 33 | 500 | ~200 | 1.4 | Yes | 0.22 | 0.1 |
| 2 | 60 | 300 | ~200 | 1.4 | Yes | 0.36 | 0.21 |
| 3 | 60 | 500 | ~200 | 1.4 | Yes | 0.21 | 0.097 |
| 4 | 60 | 1000 | ~200 | 1.4 | Yes | 0.18 | 0.052 |
| 5 | 60 | 10000 | ~200 | 1.4 | Yes | 0.205 | 0.049 |
| 6 | 60 | 1000 | ~200 | 1400 | Yes | 0.17 | 0.058 |
| 7 | 60 | 1000 | ~200 | 1.4 | No | 0.19 | 0.054 |

generally true for post-irradiation deformed metals and alloys. If the applied axial stress is smaller than about 1.5 times the matrix CRSS, the matrix critical shear stress is not influential either (Fig. 11a, for aspect ratio $L/h$ = 200). In this regime, the surface slip varies linearly with respect to the applied stress. But for higher applied stresses, the influence of the matrix threshold is noticeable and plastic slips increase with respect to the applied stress more quickly than linearly. For a given stress, the softer the matrix is, the higher the channel plastic slip is. This slip acceleration seems to occur when the matrix in the vicinity of the grain boundary and channel corners starts to deform plastically as well, i.e. when the matrix critical shear stress is reached near the grain boundary because of stress concentration (see Section 4.3.2). Matrix primary slip values in the vicinity of the grain boundary reach a few $10^{-3}$,

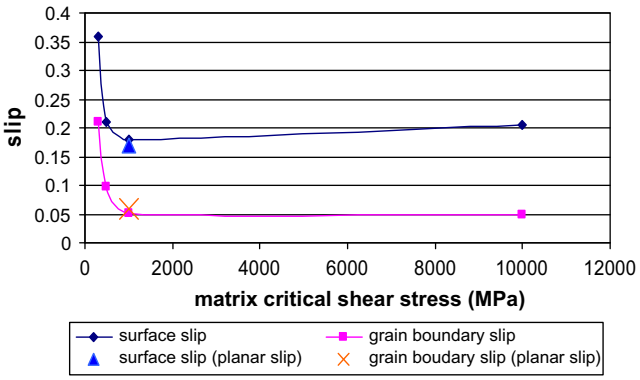


**Fig. 12.** Influence of the matrix critical shear stress on the surface and grain boundary slips. Channel critical shear stress, $\tau_{c,channel}$ = 60 MPa. Austenitic steel, 300 °C. Macroscopic axial stress: 780 MPa. Channel/matrix mesh, $L/h$ = 15.

and then increase with increasing macroscopic strain. In fact, the grain boundary slip is more sensitive to the matrix critical shear stress than the surface slip (Fig. 11b). For small aspect ratio channels ($h/L$ = 15), similar trends are observed (Fig. 12). But, the influence of the matrix critical shear stress is noticeable only for higher applied stresses (~600 MPa). An additional FE computation using a mesh with a large width (perpendicularly to Fig. 7a) was carried out. This configuration is closer to plane strain conditions than plane stress condition of the usual thin mesh. It gives mean surface slip values close to the one computed with a thin mesh. Comparisons between FE and analytical modelling [19] are discussed in Section 4.3.2.

Crystalline elasticity or isotropic elasticity give the same results provided both channel(s) and matrix obey the same law and the same remote stress is applied.

### 3.3. Influence of some microstructure parameters

The mesh used for obtaining the results described above seems rather coarse with respect to real microstructures (Fig. 1). Therefore, the influences of several microstructure parameters are now investigated in order to check the validity of the results. First, the angle between the grain boundary and the loading axis can vary between 0° and 90°. The first angle corresponds to the previous computations (Fig. 7b), whereas the second one to the probably more favourable to crack nucleation [28]. Fig. 8 shows an intermediate configuration with an angle of 45°. Second, several channels are usually observed in the same grain [5,21], which requires studying the effect of (at least) one parallel channel on the strain/stress concentration. Third, the channel thickness generally varies over a range that is non-negligible [5,21]. Following the computation results of [19], an effect of the channel aspect ratio

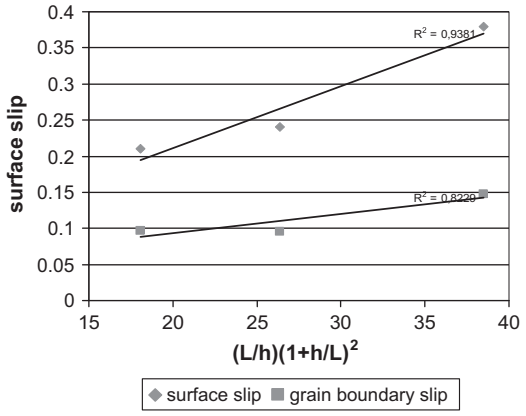


**Fig. 13.** Plots of the surface and grain boundary slip as a function of a geometrical parameter linked to the channel aspect ratio, $L/h$. Finite Element computations and linear interpolations. $R$: correlation coefficient. Channel/matrix critical shear stresses: $\tau_{c,channel}$ = 50 MPa/$\tau_{c,matrix}$ = 500 MPa. Austenitic steel, 300 °C. Macroscopic axial stress: 780 MPa.

(ratio between the length and thickness) on the surface channel slip is expected. The results of these investigations are summarized in the following paragraphs.

The angle between the grain boundary and the macroscopic axis was found to have no influence on the channel deformation (maximum values, mean surface step), except concerning the slip fields in the vicinity of the grain boundary.

Using the range of measured channel spacing given by [5], the influence of a neighbouring parallel channel was investigated in the small strain range. The inter-band spacing, $d$, ranged from 0.7 μm to 3 μm, whereas the channel thickness, $h$, was set equal to 0.7 μm (Fig. 8). In fact, the effect of the additional parallel channel seems to be rather weak, at least for a small applied stress. If two channels are taken into account instead of only one, the relative increase of the mean surface slip is only +10%.

Considering the experimental distribution of the channel thickness, $h$, given by [5], three different thicknesses were considered: 0.7 μm, 0.55 μm and 0.35 μm, while the length, $L$, was set at a constant 10 μm. As shown in Fig. 13, the clear band thickness is important on the surface and grain boundary slips. For a given grain size $L$, the narrower the clear band, the higher the mean surface and grain boundary slips (Fig. 13). The slips are plotted with respect to a geometrical factor, $(L/h)(1 + h/L)^2$, which is close to the channel aspect ratio, $L/h$, if $L/h \gg 1$. This geometrical factor arises from Eshelby's analysis of the inclusion problem [17,19] (see Section 4.1). Surface mean slips are roughly proportional to the aspect ratio, $L/h$, which permits easy extrapolation. The larger the aspect ratio, the higher the surface or grain boundary slip step.

## 4. Discussion

Predictions based on the previous finite element results are now discussed with respect to either analytical formula or experimental surface and bulk slip measures, followed by their implication for micro-crack initiation.

### 4.1. Comparison with analytical modelling

As mentioned in the introduction, the solution of the bulk inclusion problem given by Eshelby [17] allowed several authors to propose evaluations of the mean channel plastic slip [16]. They considered either thin extruded lamellae or penny-shapes with high $L/h$ aspect ratios, embedded in an elastic infinite matrix. Uniform elasticity isotropy is used. The inclusion is subjected to a uniform free strain which represents the plastic slip on the primary slip system. The induced primary shear back-stress is deduced from the value of the plastic slip. The channel obeys planar slip and perfect plasticity (critical shear stress: $\tau_{c,channel}$). The primary Schmid factor is denoted as $f$. And the hypothesis of plane strain is often made. The formula obtained using Eshelby's analysis is valid only for bulk channels [16]:

$$\gamma^p = (1-\upsilon)\frac{L}{h}\left(1+\frac{h}{L}\right)^2 \frac{f\Sigma_{xx} - \tau_{c,channel}}{\mu} \quad (5)$$

with $\mu$ the elastic shear modulus (isotropic elasticity).

The case of surface slip bands was investigated by crystalline FE computations [18–20]. It was shown that the simple use of both surface concentration coefficient, $r_{surface}$, and bulk evaluation allows a reasonable evaluation of the surface band slip [19]. For a large range of aspect ratios (10–100), a coefficient $r_{surface} \approx 1.9$ was found for type B slip bands (Schmid factor: 0.5 and shearing through the free surface with an angle of 45°) [19]. The mean slip band plastic slip is computed as follows:

$$\gamma^p = r_{surface}(1-\upsilon)\frac{L}{h}\left(1+\frac{h}{L}\right)^2 \frac{0.5\Sigma_{xx} - \tau_{c,channel}}{\mu} \quad (6)$$

To assess whether or not this formula could be used in more general cases (elasticity anisotropy, yielding in the matrix near the grain boundary, multiple slip instead of imposed single slip, various materials ...), many FE computations were carried out, considering many different materials, channel aspect ratios, applied stresses. Fig. 14 allows the comparison between the surface slip computed either analytically or numerically (FE). A perfect agreement between both estimations corresponds to the drawn line. It can be observed that both predictions are generally close, which means that analytical predictions are generally reliable. But, for high applied stresses and rather low matrix critical shear stresses, the surface primary slips computed by the FE method are higher than the analytical values, because of the yielding in the matrix in the vicinity of the grain boundary and channel/slip band bottom. Following our numerous FE computations using different aspect ratio and matrix CRSS values, the analytical formula is valid provided the applied axial stress is smaller than 1.5 times the matrix CRSS.

For a well-oriented slip system (Schmid factor = 0.5) for which shearing occurs in the free surface (type A facet), the surface ratio is equal to 1. This means that there is no difference between bulk slip band of length $2L$ and surface slip band of length $L$ [19]. For other cases, particularly for smaller Schmid factors, additional FE

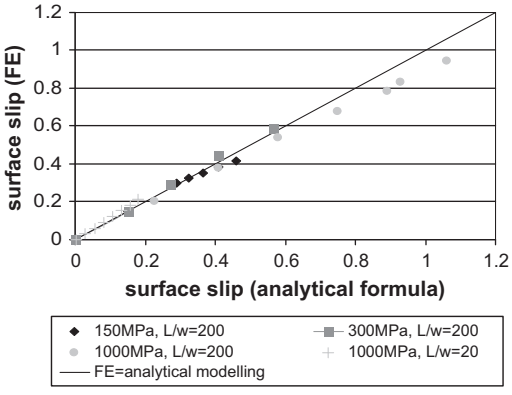


**Fig. 14.** Plots of the surface slips computed by FE for various aspect ratios, matrix critical shear stress and applied stress as a function of the surface slips computed using the analytical formula (Eq. (6)). Austenitic stainless steel, 300 °C. Channel critical shear stress, $\tau_{c,channel}$ = 50 MPa. Channel/matrix mesh.

computations are required. Nevertheless for Schmid factors close to 0.5, no strong difference is expected.

### 4.2. Comparison with surface slips measured by AFM and bulk slip measured by TEM

#### 4.2.1. Comparison with surface slips as measured by AFM

Recently Jiao et al. used AFM for measuring surface steps induced by channel deformation, from which they calculated slip values [5]. Proton-irradiated material of 1 or 5.5 dpa (306 °C) was tensile tested to an applied plastic strain of 3% (280 °C), at a low strain rate of $3.5 \times 10^{-7}$/s. The corresponding stress values were deduced from tensile curves obtained by Pokor et al. for a similar material at various neutron irradiation doses [37]. Following [42], the tensile curves measured on austenitic stainless 304 and 316 pre-irradiated at the same dose using either proton or neutron are very similar. Jiao et al. measured the fraction of surface grains showing channelling, as visible in scanning electron microscope images [5]. For doses of 1 and 5.5 dpa, the grain fractions were 30% and 50%, respectively. Following the observations reported in [15,26], the grains exhibiting channelling were generally well-oriented (high Schmid factor values). Using the cumulated probabilities of the Schmid factor for a FCC polycrystal without texture, the average Schmid factors of the most well-oriented grains were estimated to be 0.49 for 30% and 0.48 for 50% [41]. One-half of the channels are assumed to be of type B and one-half of type A. Then the applied formula differ somewhat. For type B channels, Eq. (6) is applied, but using a 3D correction factor of 1/1.3 because Eq. (6) is valid for plane strain condition whereas the channel depth in the $y$ direction is finite and equal to the grain size. The correction factor is computed from Fig. 6 of [19] which gives the plastic slip depending on the length along the $y$ direction. If the length along $y$ is equal to the grain size, then the plastic slip is 1.3 times smaller than if this length is infinite (plane strain condition). For type A channels, the same 3D correction is applied to Eq. (5). The grain size is about 20 μm [5]. And the channel thickness is about 50 nm following the TEM images plotted in [43]. All the parameters required for computations (slip band aspect ratio, slip band critical shear stress) are given in Table 4. Following Fig. 15, the agreement is rather encouraging because no adjustable parameter is used. Nevertheless, some remarks should be mentioned. Only the orders of magnitude could be compared, because computations should be carried out for other orientations and Schmid factor values. Orientations, grain sizes and channel/slip band thicknesses are indeed generally variable at the polycrystal surface and the influence of the neighbour grains is non-negligible, as shown in [41]. In addition, the high values of the matrix critical shear stress employed induce only local yielding in the vicinity of the grain boundaries. The influence of the plastic flow of the matrix should be further investigated because the macroscopic plastic strains are generally non-negligible in these experiments. Jiao et al. observed channel expansion close to the grain boundaries [43]. The channels become wider close to the GBs, which could affect the local plastic slip. But, this expansion mechanism should not affect the mean channel value as the expansion area length is lower than 1 μm which is much lower than the grain size, $L$.

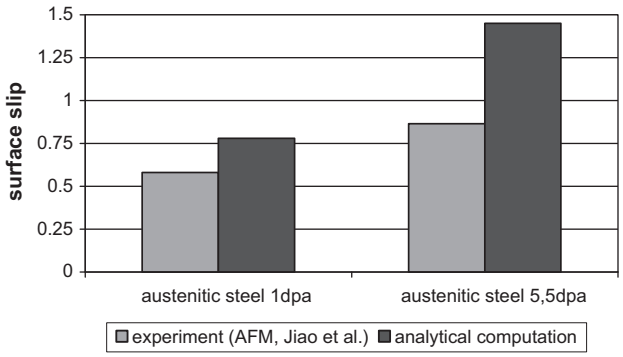


**Fig. 15.** Comparison between surface slips either obtained by AFM measurements [5] or computed using the analytical formulae (surface channels, see Section 4.2). 304L, proton pre-irradiation, applied axial strain: 3%. The parameters used for the computations are given in Table 3. They have been deduced either from the microstructural investigations described in [3–6] or the tensile curves of similar 304L depending on the irradiation dose [37,42].

#### 4.2.2. Comparison with bulk channel slips measured by TEM

Similar analytical computations are carried out using Eq. (5), which is valuable for bulk channels. As previously, a correction of 1/1.3 is made based on Fig. 11 of [19]. Then the computed slips could be compared to the values measured using the TEM pictures (Figs. 3 and 4). Shearing of some of the channels induced displacements of either crossed channels or dislocations. The incident beam vector is equal to [−1 1 0]. As the slip planes are perpendicular to, let us say, the [1 1 −1] vector, the displacements evaluated in Figs 3 and 4 (white arrows, Section 2.1) correspond to displacements along the [1 1 2] vector, which is perpendicular to both [−1 1 0] and [1 1 −1] vectors. It is supposed that only one slip system is activated along the {1 1 −1} slip plane. The corresponding Burgers vector is either [−1 1 0] or [0 1 1], and not [−1 1 0] which is the incident beam vector. The displacements along the possibly activated Bürgers vectors are obtained after dividing the displacements measured in Figs. 3 and 4 by a factor cos(30°). The angles between the possibly activated Bürgers vectors and the [1 1 2] vector are in fact equal to ±30°/±150°. No correction on the thicknesses measured in Section 2.1 is needed because they were measured along the [1 1 −1], which is perpendicular to the incident beam vector, [−1 1 0]. The displacements along the possibly activated Bürgers vectors are finally divided by the measured thicknesses. The displacements along the Bürgers vectors, channel thicknesses and slip values are given in Table 5, corresponding to the arrows plotted in Figs. 3 and 4. The error bars are given as well. The displacements are presumed to occur along the Burgers vector, because the channels are easily observable. The applied tensile stress is given, along with its error range. An average value of the Schmid factor is used, as no precise information is available concerning the crystallographic orientations of the grains. The average value considering a FCC polycrystal without texture is about 0.45. An error range of ±0.05 is used in addition. Following the Schmid factor distribution curve, 100% of the grains present a Schmid factor smaller than 0.5% and only 10% a Schmid factor smaller than 0.4. Computed and measured slips with the corresponding error

**Table 4**
Material and loading parameters (applied axial stress, critical shear stresses and microstructure) used for computations leading to Fig. 14 (comparison between computed surface slips (see Section 4.2) and surface slips measured by AFM by Jiao et al. [5]).

| Pre-irradiation [5] | Remote stress (MPa) [37,42] | Fraction of surface grains presenting channels [5] | Corresponding average Schmid factor, $f$ [41] | $\tau_{c,channel}$ (MPa) [31–33] | $\tau_{c,matrix}$ (MPa) | Grain size, $L$ (μm) [5] | Channel thickness, $h$ (nm) [43] |
|---|---|---|---|---|---|---|---|
| Proton irradiation 1 dpa | 450 | 30% | 0.49 | 30 | 1000 | 20 | 50 |
| Proton irradiation 5.5 dpa | 800 | 50% | 0.48 | 30 | 1000 | 20 | 50 |

**Table 5**
Parameters (applied axial stress, critical shear stresses and microstructure) used for measurements and computations of bulk slips corresponding to the TEM pictures displayed in Fig. 3 and 4 (see Section 4.3). Critical shear stresses: $\tau_{c,channel}$ = 30 MPa.

| Grain | Remote stress (MPa) | Grain size, $L$ (μm) | Channel thickness, $h$ (nm) | Schmid factor | Measured displacement (nm) (⟨112⟩ direction) | Experimental slip (per clear band average) | Computed slip Eq. (5) |
|---|---|---|---|---|---|---|---|
| Fig. 3 | 175 (±25) | 100 | 52 (±8) | 0.45 (±0.05) | 70 (±8)<br>70 (±8)<br>65 (±8) | 1.5 (±0.35) | 0.8 (±0.55) |
| Fig. 4 | 175 (±25) | 100 | 40 (±5) | 0.45 (±0.05) | 70 (±5)<br>55 (±5) | 1.8 (±0.3) | 1.0 (±0.7) |

bars are plotted in Fig. 16. The orders of magnitude are the same (∼100%). It is difficult to improve the agreement between predictions and measures without quantitative evaluation of the macroscopic stress and grain sizes/the Schmid factors of the two studied grains. Work is in progress for improving the accuracy of the parameters used by the model which is rather sensitive to the grain size for example (Eqs. (5) and (6)). This should allow more precise comparisons with slips measured in particular grains.

### 4.3. Crack initiation mechanisms

Dislocation channel deformation, as with other localization mechanisms, induces surface strain concentration and consequently grain boundary stress concentration. This could be expected to promote grain boundary crack initiation, and is therefore an important factor that could contribute to irradiation assisted stress corrosion cracking (IASCC).

#### 4.3.1. Fracture of the surface oxide layer

During tensile loading in a LWR environment, a passive oxide layer forms on the surface of the austenitic stainless steel specimen, limiting uniform corrosion. If this oxide layer is fractured as a consequence of deformation in the underlying alloy, water can access and locally oxidizes the bare metal. The process of repeated fracture of the passive layer and following re-oxidation of the metal is the central principle of the so-called slip-dissolution or slip-oxidation models [44,45]. The oxide brittle fracture strain is denoted as $\varepsilon_{f,\text{oxide}}$. The surface channel strain, $\varepsilon_{xx,\text{channel}}$, is one-half of the plastic slip, $\gamma^p$, (the vectors defining the well-oriented slip system form an angle of 45° with respect to the tensile axis, $x$). If the macroscopic behaviour is elastic, the macroscopic axial strain can be easily evaluated by $E_{xx} = \sum_{xx}/Y$, where $Y$ is the Young's modulus. The time required for oxide fracture is equal to $\varepsilon_{f,\text{oxide}}/(\mathrm{d}E_{xx}/\mathrm{dt})$ if channelling is neglected and $\varepsilon_{f,\text{oxide}}/(\mathrm{d}\varepsilon_{xx,\text{channel}}/\mathrm{dt})$ if channel deformation is taken into account. Viscosity is negligible for austenitic stainless steels at about 300° [30,31], so only rates with respect to the loading parameter are considered. Following Eq. (6), the plastic slip and axial strain vary rather linearly with respect to the applied strain, $E_{xx}$. Under constant elongation rate test condition, the ratio of the required number of oxide failures with and without channelling is equal to $(\varepsilon_{xx,\text{channel}}/E_{xx})$, which is plotted in Fig. 17 (exponent: $m = 1$). Following the above results (see Section 3.3), this ratio is proportional to the channel aspect ratio, $L/h$. For usual values ($L/h > 200$), this ratio is higher than a few hundred, which means a strong acceleration of oxide layer fracture. Following the slip-oxidation model [44,45], short crack propagation rate, da/dt, is proportional to either $((\mathrm{d}E_{xx}/\mathrm{dt})/\varepsilon_{f,\text{oxide}})^m$ (no channelling) or $((\mathrm{d}\varepsilon_{xx,\text{channel}}/\mathrm{dt})/\varepsilon_{f,\text{oxide}})^m$ (channelling), with m the exponent of the decay of the current density at each repeated oxide fracture and re-oxidation of the bare surface. In the case of strain-controlled tests, the ratio of crack propagation rates with and without channelling is equal to $(\varepsilon_{xx,\text{channel}}/E_{xx})^m$. Following [45], the values of m usually belong to the range 0.3–1, depending on the material and environment conditions. The values computed for the typical exponent values are plotted in Fig. 17. If the m value is high (∼0.8), the crack propagation rate is multiplied by a few hundred for the typical channel aspect ratio of $L/h > 200$. But if the m value is very low (∼0.3), then the crack propagation rate is only increased by a factor of 5–10. Therefore, if the slip oxidation is involved in the damage process, channelling leads to considerably higher predicted GB crack nucleation time and crack propagation rates. The effect depends quantitatively on both channel aspect ratio, $h/L$, and m exponent. .It should be noticed that the channel slip computations and therefore the strain concentration coefficient evaluation do not take into account the influence of the oxide layer on the mechanical point of view. Following the FE computations

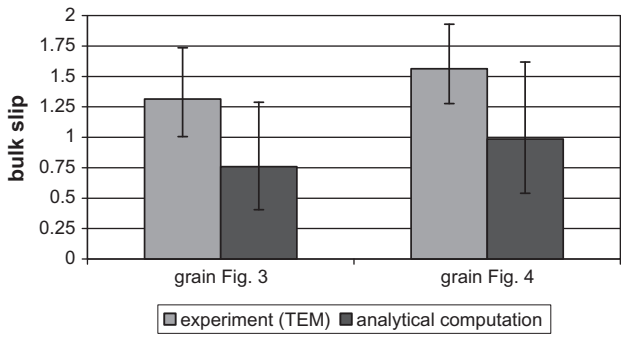


**Fig. 16.** Comparison between measured slips inside channels. Measures obtained using TEM pictures (Figs. 3 and 4, Table 4). Computed values obtained using the analytical formula valuable for bulk channels (see Section 4.3). Material and loading parameters given in Table 4 are used for computing average, minimum and maximum bulk slip values.

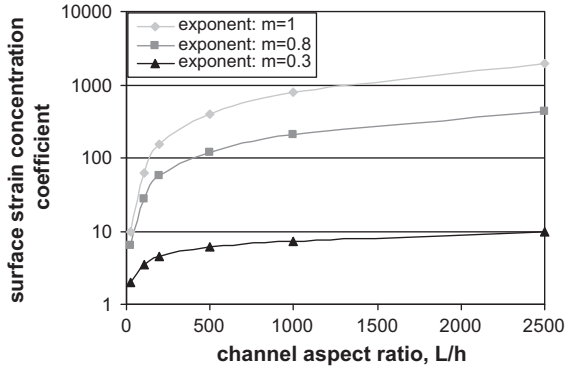


**Fig. 17.** Localization concentration coefficient, $(\varepsilon_{xx,\text{channel}}/E_{xx})^m$, depending on the channel aspect ratio, $L/h$; For $m = 1$, this correspond to the strain concentration coefficient. For $0.3 < m < 0.8$ ($m$: exponent of the decay of the oxidation current density) [45] and if channelling occurs, this coefficient affects directly the short crack propagation rate. Logarithmic scale. Application of the slip-oxidation model [44,45]. Eq. (6) is used for computing the maximum tensile strain at the free surface of a channel, $\varepsilon_{xx,\text{channel}}$ (type B, i.e. emerging at the free surface with an angle of 45°, Fig. 6b). The macroscopic axial strain, $E_{xx} = \sum_{xx}/Y$, is computed supposing that the macroscopic behaviour is purely elastic. Austenitic stainless steel, 300 °C.

for the effect of an oxide layer above a slip band embedded in a matrix [20], the channel surface slip would be about one-half smaller if the material surface had an oxide layer having a thickness equal to the channel thickness. But the channel slip would nevertheless be much higher than the macroscopic axial strain.

*4.3.2. Stress concentration at grain boundaries and crack initiation mechanisms*

The stress iso-value plots show that channel impingement at grain boundaries (GBs) induces high stress concentrations close to the GBs (Fig. 18). If we consider the irradiation and loading conditions of our TEM study, and a typical value of channel aspect ratio of 200 (channel thickness: $h \sim 50$ nm and grain size: $L \sim 10$ μm), then the normal stress at the GB perpendicular to the loading axis is eight times higher than the remote stress if the distance to the channel is smaller than one-tenth of the channel thickness $h$. It is four times higher provided the distance is smaller than one-half of the thickness. Following the stress fields computed for aspect ratios of either 15 or 200, the higher the aspect ratio, the greater the stress concentration. The stress triaxiality, defined as the ratio between the pressure and the von Misès stress, is considerably increased in the vicinity of the grain boundary. It is indeed about three times higher than the macroscopic one if the distance to the channel is smaller than one-tenth of the channel thickness. Computations using a finer mesh size close to the grain boundary show that the maximum stress value depends slightly on the mesh size (relative variation of about 25%), even if the amount of grain boundary slip does not, as shown by Fig. 11a. The TEM observations of Edwards on irradiated pure copper show that local lattice rotations arise at the intersections of channels/twins and grain boundaries [46], which they link to local stress concentrations. In addition, Onchi et al. observed that linear features and deformation twins in irradiated 304 stainless steel induce micro-twinning close to GBs [14], offering indirect evidence of these local stress concentrations. From the modelling point of view, stress concentrations have been studied for a long time in the context of considering pile-ups of individual dislocations [47]. Channel thicknesses are generally not negligible ($20\text{ nm} < h < 100\text{ nm}$) and many slip planes are included in each channel (about 10 or more). This means that each channel could contain several pile-ups. For computing the stress field induced by the pile-ups, both their number and the number of dislocations in each are needed. The predicted values of these numbers are still missing even if the total number of dislocations could be deduced from the computed channel plastic slip. In the framework of continuum modelling, the local stress gradients at grain boundaries and triple points have been evaluated using thermo-elasticity modelling [48,49]. However, the local gradients of plastic strain tensors are not taken into account in each grain where the plastic strain is supposed to be homogeneous. This leads to a logarithmic dependence of the stress with respect to the distance to the triple point, which is probably overestimated. Finally, recent crystalline FE computations have shown that high stress concentrations arise at GBs due to incompatibility of plastic strain tensors [50].

Local stress concentrations could be expected to accelerate local damage mechanisms. In pressurized water reactor (PWR) or boiling water reactor (BWR) water environments, corrosion processes are active. Diffusion of oxygen or hydrogen may occur along grain boundaries, most likely along general grain boundaries. This would decrease the grain boundary cohesion strength and fracture energy. Such a mechanism has been proposed by Scott for alloy 600 in PWR environment [51], and could also be relevant to other alloys, provided grain boundary diffusion was sufficiently rapid. Following the molecular dynamics computations of Van der Ven and Ceder [52], a fraction of 40% of oxygen atoms in a {1 1 1} aluminium plane induces a relative decrease of a factor of two in the cohesion strength. The same fraction of hydrogen atoms induces a decrease of a factor three. As at distance of one-tenth of the channel thickness, the GB normal stress is about eight times higher than the applied stress (equal to the yield stress). For high irradiation dose, the yield stress is about 800–1100 MPa [37,42]. Therefore, the GB stress is higher than 6000 MPa whereas the theoretical cleavage stress is about $Y/10$, that is 17,000 MPa [27]. If oxygen or hydrogen effect is taken into account as well, the critical brittle fracture stress could be reached along a segment of GB of about one-tenth of the channel thickness.

Nevertheless, several experimental studies have shown that an environment effect is not necessary for obtaining intergranular damage during slow strain rate tensile loading of pre-irradiated austenitic stainless steels. After irradiation of respectively 1.7 dpa in BWR and 30 dpa in PWR, the tensile tests in 290 °C inert gas of Onchi et al. [14] and in 340 °C argon of Toivonen et al. [12] lead to partial intergranular fracture. Further, Lim and Raj observed cavitation at grain boundaries in pure (unirradiated) nickel polycrystals in vacuum ($10^{-5}$ Pa) at 300 °C, reportedly induced by slip band impingement during cyclic tests carried out on [53]. On the

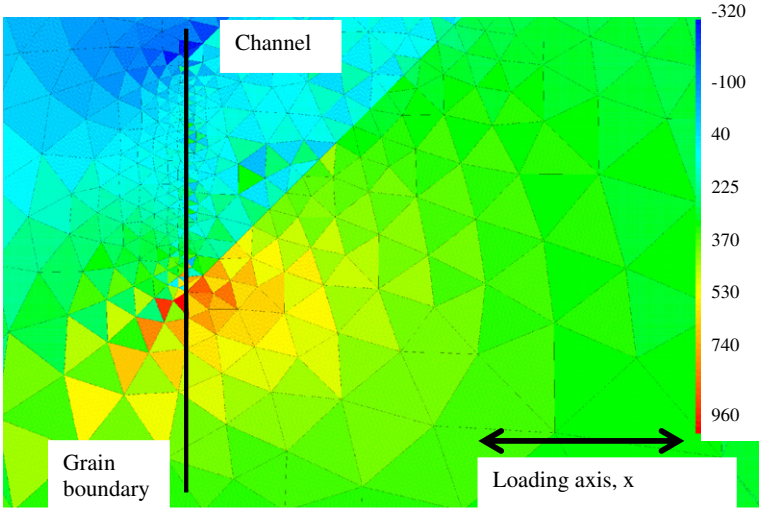


**Fig. 18.** Isovalues of the stress normal to the grain boundary, $\sigma_{xx}$ (MPa). FE computation using the refined mesh. Parameters: $\tau_{c,channel} = 30$ MPa, $\tau_{c,matrix} = 300$ MPa, austenitic steel, 300 °C, $L/h = 200$, grain boundary angle with respect to the loading axis: 90°, applied tensile stress: $\sum_{xx} = 120$ MPa.

one hand, radiation induced segregation (RIS) could eventually affect the cohesion strength of grain boundaries. On the other hand, cavitation could occur because of stress gradient and diffusion of vacancies along general GBs, which is accelerated with respect to bulk diffusion. Raj proposed a model of cavitation initiation [54]. He computed the time required for initiating a stable cavity from the energy point of view, calculating a critical radius as $r_c = 2\gamma_s/\sigma_n \sim 1$ nm ($\gamma_s \sim 1$ J/m$^2$ and $\sigma_n \sim 8$ times the macroscopic stress if $r < h/10$). The critical time was found to be inversely proportional to the power four or five of the stress around the cavity [54]. Localization would therefore decrease the initiation of small cavities by a factor higher than 1000.

These two crack initiation mechanisms could explain why, during stress corrosion tests [55,56] and in inert environment tests [53], cavities and cracks appear preferentially along general grain boundaries. Along these kinds of GBs the diffusion of vacancy or interstitial atoms is generally considered to be much faster than along special grain boundaries (such as twins) and in the bulk [57].

These results concerning the application of the slip-oxidation model, brittle fracture of grain boundaries affected by environment and cavity nucleation due to vacancy diffusion indicate why dislocation channel deformation could be expected to strongly accelerate the damage mechanism kinetics, often by a factor of a few hundred or more. They are in agreement with recent experimental results reported in the literature showing the influence of slip localization on intergranular damage:

- Couvant et al. observed cavities directly at the intersections of shear bands and GBs at the surface of a cold-worked material subjected to a stress corrosion test in PWR environment [58].
- Bailat et al. [59] compared the stress corrosion cracking (SCC) susceptibility of pre-irradiated 304L and 316L stainless steels. They explained the lower resistance of 304L because of its stronger tendency to deformation localization due to a lower stacking fault energy (SFE) value than 316L.
- Jiao et al. [43] compared the SCC susceptibility of three different 304L presenting various stacking fault energy values in PWR and BWR water. They concluded that the lower the SFE, the higher the deformation localization and the higher the SCC susceptibility.
- Teyserre et al. [60] compared two alloys, 316L and nickel-base alloy 690, and concluded that neither RIS nor irradiation hardening correlates with SCC susceptibility in supercritical water. In addition, as noticed above, intergranular damage has been observed in pre-irradiated austenitic stainless steels loaded at low strain rate in inert environment at about 300 °C [12,14], which means that environment effect is not always necessary.
- Slip lines are usually observed on the grain boundaries located on the intergranular fracture surfaces whatever the tensile test environment [14,16,43].
- The recent experimental study of Savoie et al. showed that precipitation-hardened austenitic steel A286 is more sensitive to SCC in PWR water if initial slip bands are present at the beginning of the stress corrosion test than if there is none [61]. The slip bands were formed by preliminary cyclic loading in order to shear and dissolve fine gamma-prime precipitates hardening the matrix on the principle slip planes.

Finally, the influence of irradiation dose on channel thickness should be discussed. Following the previous modelling results, the channel aspect ratio is a very influential value. The thinner the channel, the higher the induced slip and stress concentrations. But the literature results concerning the influence of irradiation on channel thickness do not agree. Following Sharp's observations on copper single crystals [1], the higher the dose, the thinner the channels. On the contrary, the observations of Farrell et al. on 316L polycrystals [62] showed the opposite influence. From the experimental point of view, it seems clear that the higher the dose, the more efficient the IASCC damage, even if for example irradiation defects and hardening are effectively saturated with respect to the dose (higher than a few dpa for example).

One potential explanation for the apparent disagreement could be that the degree of accumulated strain could also encourage expansion (thickening) of the channels. This has also been indicated by the MD and DDD modelling of Nogaret et al. [9]. With lower dose, the defects are "weak", so the channels may remain narrow on account of the fact that only a small amount of strain can accumulate before strain hardening raises the stress to a level that exceeds the threshold stress for localization, thus ending the strain localization. Around 1 dpa it would be reasonable that the channel thickness may be more sensitive to accumulated strain, such that an apparent broadening in thickness with increasing dose would actually be due to the fact that the higher dose could sustain localization to a higher level of accumulated strain before strain hardening at channel intersections raised the stress to threshold level, enabling the channels to thereby broaden during that period. On the other hand, at a higher dose the stress required to maintain localization may be greater, counteracting both the broadening and exceeding the stress required to initiate new channels or to induce grain boundary cracking.

## 5. Conclusions

Transmission electron microscopy (TEM) observations have shown that channelling occurs in deformed, pre-irradiated austenitic stainless steels, even for low neutron dose (~0.16 dpa, 185 °C) and stress (~175 MPa, 290 °C). Exploiting the TEM observations, finite element (FE) meshes were designed that included one or two channels of "soft" material, i.e. having a low CRSS, embedded at the free surface of a "hard" matrix volume, i.e. with a high CRSS. The CRSS were adjusted using experimental data, such as yield stress and hardening curve of recovered 316L single crystals and physically based models such as Orowan's critical stress or molecular dynamics from the literature. For doses leading to hardening saturation, the computed surface slips were as high as 100% for applied stress close to the yield stress when the aspect ratio (length divided by thickness) of the observed channels was used. Surface slips were much greater than the grain boundary slips because of matrix constraint effect. The matrix CRSS and the channel aspect ratio were the most influential material parameters. Predictions based on an analytical formula were compared with surface slips computed by the FE method, and their validity domain was evaluated, corresponding to a remote axial stress smaller than 1.5 times the matrix CRSS. The surface slip in such conditions was proportional to the channel aspect ratio. Based on the measured channel aspect ratios and applied stresses, slips were computed either in surface or bulk channels. As no adjustable parameter is used, the comparison with corresponding atomic force microscopy measurements reported in the literature or measurements based on our TEM observations seems encouraging. Finally, it was shown that the induced surface slip and grain boundary stress concentrations accelerated the kinetics of the damage mechanisms possibly involved in IASCC.

## Acknowledgments

The authors thank CEA (DEN-DSOE) and the European project PERFECT for financial support (Contract number: F160-CT-2003-508840). We are grateful to Dr. Lionel Fournier and Dr. Benoît Tanguy for interesting discussions.

## References


[1] J.V. Sharp, Philos. Mag. 16 (1967) 77.
[2] M. Victoria, N. Baluc, C. Bailat, Y. Dai, M.I. Luppo, R. Schäublin, B.N. Singh, J. Nucl. Mater. 276 (2000) 114.
[3] E.H. Lee, T.S. Byun, J.D. Hunn, K. Farrell, L.K. Mansur, J. Nucl. Mater. 296 (2001) 183.
[4] D.J. Edwards, B.N. Singh, J.B. Bikde-Sorensen, J. Nucl. Mater. 342 (2005) 164.
[5] Z. Jiao, J.T. Busby, R. Obata, G.S. Was, in: T.R. Allen, P.J. King, L. Nelson, (Eds.), Proceedings of the 12th International Conference on Environmental Degradation of Materials in Nuclear Power Systems – Water Reactors, The Minerals, Metals and Materials Society, Warrendale, PA, 2005, pp. 379.
[6] T.S. Byun, N. Hashimoto, K. Farrell, J. Nucl. Mater. 351 (2006) 303.
[7] E.H. Lee, M.H. Yoo, T.S. Byun, J.D. Hunn, K. Farrell, L.K. Mansur, Acta. Mater. 49 (2001) 3277.
[8] Y.N. Osetsky, R.E. Stoller, D. Rodney, B.J. Bacon, Mater. Sci. Eng. A 400–401 (2005) 370.
[9] Th. Nogaret, Ch. Robertson, D. Rodney, Philos. Mag. 87 (2007) 945.
[10] D.J. Edwards, B.N. Singh, J. Nucl. Mater. 329–333 (2004) 1072.
[11] E.P. Simonen, S.M. Bruemmer, in: A.R. McIllree, S.M. Bruemmer (Eds.), Proceedings of 7th International Symposium on Environmental Degradation of Materials in Nuclear Power Systems – Water Reactors: National Association of Corrosion Engineers, vol. 2, Houston, TX, 1995, p. 1.
[12] A. Toivonen, U. Ehrnsten, W. Karlsen, P. Aaltonen, J.P. Massoud, J.M. Boursier, in: T.R. Allen, P.J. King, L. Nelson, (Eds.), Proceedings of the 12th International Symposium on Environmental Degradation of Materials in Nuclear Power Systems – Water Reactors, Warrendale, PA, 2005, p. 327.
[13] H.M. Chung, R.V. Strain RV, W.J. Shack, Nucl. Eng. Des. 208 (2001) 221.
[14] T. Onchi, K. Dohi, N. Soneda, J.R. Cowan, R.J. Scowen, M.L. Castano, J. Nucl. Mater. 320 (2003) 194.
[15] S.M. Bruemmer, E.P. Simonen, P.M. Scott, P.L. Andresen, G.S. Was, J.L. Nelson, J. Nucl. Mater. 274 (1999) 299.
[16] K.V. Rasmussen, O.B. Pedersen, Acta Metall. 14 (1980) 1467.
[17] J.D. Eshelby, Proc. Roy. Soc. Lond. A 241 (1957) 376.
[18] E.A. Repetto, M. Ortiz, Acta Mater. 45 (1997) 2577.
[19] M. Sauzay, P. Gilormini, Theor. Appl. Fract. Mech. 38 (2002) 53.
[20] M. Sauzay, C. Caës, M. Mottot, Ch. Robertson, J. Phys. IV France 106 (2003) 99.
[21] W. Karlsen, K. Dohi, T. Onchi, in: Proceedings of the 13th International Conference on Environmental Degradation of Materials in Nuclear Power Systems, Canadian Nuclear Society, CNS, 2007.
[22] J.W. Brooks, M.H. Loretto, R.E. Smallman, Acta Metall. 27 (1979) 1839.
[23] M. Sauzay, P. Gilormini, Fatigue Eng. Mat. Struct. 23 (2000) 573.
[26] F. Onimus, I. Monnet, J.-L. Béchade, C. Prioul, Ph. Pilvin, J. Nucl. Mater. 328 (2004) 165.
[27] F.A. Mc Clintock, A.S. Argon, Mechanical Behaviour of Materials, Addison-Wesley Publishing Company, 1996.
[28] H.B. Huntington, in: F. Seitz, D. Turnbull (Eds.), Solid State Physics, vol. 7, Academic Press Corporation Publishers, New-York, 1958, p. 214.
[29] L. Anand, S. Balasubramanian, K. Kothari, in: Ch. Teodosiu (Ed.), CISM Courses and Lectures n 376, Large Plastic Deformation of Crystalline Aggregates, 1996.
[30] G. Cailletaud, V. Doquet, A. Pineau, in: K. Kussmaul, D. McDiarmid, D. Socie (Eds.), Proceedings of Fatigue under Biaxial and Multiaxial Loading, ESIS10, Mechanical Engineering Publications, London, 1991, p. 131.
[31] S. Héraud, Ph.D. Thesis, Ecole Polytechnique, Palaiseau, France, 1998.
[32] Y. Li, C. Laird, Mater. Sci. Eng. A 186 (1994) 65.
[33] C. Gorlier, Ph.D. Thesis, Ecole des Mines de Saint-Etienne, France, 2008.
[34] D.J. Bacon, Y.N. Osetsky, Mater. Sci. Eng. A 400–401 (2005) 353.
[35] C. Pokor, Y. Brechet, Ph. Dubuisson, J.-P. Massoud, X. Averty, J. Nucl. Mater. 326 (2004) 19.
[36] D. Rodney, Nucl. Instrum. Methods Phys. Res. B 1–4 (2005) 100.
[37] C. Pokor, X. Averty, Y. Bréchet, Ph. Dubuisson, J.-P. Massoud, Scr. Mater. 50 (2004) 597–600.
[38] http://www-cast3m.cea.fr
[39] H. Haddadi, S. Héraud, L. Allais, Ch. Téodosiu, A. Zaoui, in: C. Miehe (Ed.), Proceedings of the IUTAM Symposium on "Computational Mechanics of Solid Materials at Large Strains", Kluwer Academic Publishers, 2001.
[40] M. Sauzay, Th. Jourdan, Int. J. Fract. 141 (2006) 431.
[41] M. Sauzay, Acta Mater. 55 (2007) 1193.
[42] G.S. Was, J.T. Busby, T. Allen, E.A. Kenik, A. Jenssen, S.M. Bruemmer, J. Gan, A.D. Edwards, P.M. Scott, P.L. Andresen, J. Nucl. Mater. 300 (2002) 198.
[43] Z. Jiao, J.T. Busby, G.S. Was, J. Nucl. Mater. 361 (2007) 218.
[44] D.D. Mac Donald, M. Urquidi-Macdonald, Corros. Sci. 32 (1991) 51.
[45] F.P. Ford, Corrosion 52 (1996) 375.
[46] D.J. Edwards, J. Nucl. Mater. 342 (2005) 178.
[47] J.P. Hirth, J. Lothe, Theory of Dislocations, Krieger Publishing Company, Malabar, Florida, 1992.
[48] C. Rey, A. Zaoui, Acta Metall. 28 (1980) 687.
[49] S. Caré, A. Zaoui, Acta Mater. 44 (1996) 1323.
[50] O. Diard, S. Leclercq, G. Rousselier, G. Cailletaud, Int. J. Plast. 21 (2005) 691.
[51] P.M. Scott, in: Proceedings of the 9th International Symposium on Environmental Degradation in Nuclear Power Systems – Water Reactors, Newport Beach, 1999, p. 3.
[52] A. Van der Ven A, G. Ceder, Acta Mater. 52 (2004) 1223.
[53] L.C. Lim, R. Raj, Acta Metall. 8 (1984) 1183.
[54] R. Raj, Acta Metall. 26 (1978) 995.
[55] B. Alexandreanu, G.S. Was, Corrosion 59 (2003) 705.
[56] L. Tan, K. Sridharan, T.R. Allen, J. Nucl. Mater. 348 (2005) 263.
[57] A.P. Sutton, R.W. Balluffi, Interfaces in Crystalline Materials, Clarendon Press, Oxford, 1995.
[58] Th. Couvant, L. Legras, F. Vaillant, J.-M. Boursier, Y. Rouillon, in: T.R. Allen, P.J. King, L. Nelson (Eds.), Proceedings of 12th International Symposium on Environmental Degradation of Materials in Nuclear Power Systems – Water Reactors, The Minerals, Metals & Materials Society, Warrendale, PA, 2005, p. 1069.
[59] C. Bailat, A. Almazouzi, N. Baluc N, R. Schäublin, F. Gröschel, M. Victoria, J. Nucl. Mater. 283–287 (2000) 446.
[60] S. Teysseyre, Z. Jiao, E. West, G.S. Was, J. Nucl. Mater. 371 (2007) 107.
[61] L. Fournier, M. Savoie, D. Delafosse, J. Nucl. Mater. 366 (2007) 187.
[62] K. Farrell, T.S. Byun, N. Hashimoto. Mapping Flow Localization Processes in Deformation of Irradiated Reactor Structural Alloys, ORNL/TM-2003/63, September, 2003.